6.3 Summary 102

7 Bibliography **111**

List of Tables

1.1 Seismic Data volumes for 2D and 3D prestack data. 3
1.2 Storage for the full Green's functions for 2D and 3D datasets. 4
1.3 Storage for subsampled Green's functions for 2D and 3D datasets. 4
1.4 Storage for parametric Green's functions for 2D and 3D datasets. 5

List of Figures

1.1 Phase as a function of frequency for a simple dispersed event. 7
1.2 Migration using three different traveltime fields. 8
1.3 Valid frequency range of algorithms. 10

2.1 Amplitude and phase in rectangular coordinates. 15
2.2 Time slice in rectangular coordinates. 15
2.3 Amplitude and phase in polar coordinates. 17
2.4 Time slice in polar coordinates. 17
2.5 Snapshots of Green's functions in a linear gradient. 19
2.6 Paraxial modeling in rectangular and polar coordinates. 21
2.7 Modeling in a linear velocity gradient in depth. 25
2.8 Modeling in a two layer model. 26
2.9 Modeling in medium with a Gaussian anomaly. 27

3.1 Constant offset modeling in a V(z) medium 32
3.2 Adjoint modeling 33
3.3 Central trace of adjoint modeling. 34
3.4 Modeling + spherical spreading correction. 35
3.5 Adjoint modeling after spherical spreading correction. 36
3.6 Central trace of adjoint modeling after spherical spreading correction. . . . 37
3.7 Central trace of migration inversion. 39
3.8 Constant offset migration/inversion. 40

4.1 Time slice through the full Green's function in a V(z) medium. 44
4.2 Depth slice through the full Green's function in a V(z) medium. 44
4.3 Unwrapped phase curve for the superposition of two discrete events. 46

4.4 Time domain Green's function created using sparse frequency sampling. . . 48
4.5 Amplitude, traveltime and phase plots for the "blob" model. 52
4.6 Maximum energy traveltime contours superimposed on the full Green's function. 52
4.7 Time slice of the full and parametric Green's functions. 53
4.8 Depth slice of the full and parametric Green's functions. 53

5.1 The slowness model for the Marmousi dataset. 58
5.2 Traveltime contours for three methods. 61
5.3 Traveltime contours at 0.9sec. superimposed on wavefield. 62
5.4 Traveltime contours at 1.1sec. superimposed on wavefield. 63
5.5 First arriving traveltime picks superimposed on full wavefield 64
5.6 Paraxial ray tracing traveltime picks superimposed on full wavefield 65
5.7 Band-limited traveltime picks superimposed on full wavefield 66
5.8 Full wavefield and approximate wavefields at 0.7sec. 69
5.9 Full wavefield and approximate wavefields at 0.9sec. 70
5.10 Full wavefield and approximate wavefields at 1.1sec. 71
5.11 Comparison of amplitude fields from paraxial ray tracing and band-limited Green's functions. 73
5.12 Comparison of phase fields from paraxial ray tracing and band-limited Green's functions. 74

6.1 Marmousi synthetic data, shot gathers. 80
6.2 Marmousi synthetic data, near trace section. 81
6.3 Marmousi shot record before and after pre-processing. 84
6.4 Marmousi true slowness model. 85
6.5 Synthetic reflectivity section for the Marmousi model. 86
6.6 Marmousi dataset migrated using a commercial shot profile migration program. 87
6.7 Kirchhoff migration using first arriving traveltimes. 89
6.8 Kirchhoff migration using traveltime and phase maps calculated by paraxial ray tracing. 90
6.9 Kirchhoff migration using traveltime, amplitude, and phase maps calculated by paraxial ray tracing. 91

6.10 Kirchhoff migration using band-limited traveltimes and phase maps. 93
6.11 Kirchhoff migration using band-limited traveltime, amplitude and phase in an adjoint process. 94
6.12 Kirchhoff migration/inversion using band-limited traveltime, amplitude and phase maps. 95
6.13 Kirchhoff migration/inversion using low-frequency, band-limited traveltime, amplitude and phase maps. 96
6.14 CDP gathers computed using first arriving traveltimes. 98
6.15 CDP gathers computed using traveltimes and phases from paraxial ray tracing. 99
6.16 CDP gathers computed using traveltimes and phases from band-limited Green's functions. 100
6.17 Comparison of CDP gathers. 101
6.18 A simplified version of the true slowness field. 103
6.19 Kirchhoff migration/inversion using band-limited traveltime, amplitude, and phase maps calculated in the simplified model. 104
6.20 Kirchhoff migration/inversion using paraxial ray tracing traveltime, amplitude, and phase maps calculated in the simplified model. 105
6.21 Comparison of CDP gather after imaging with the true model and the simplified model. 106
6.22 Comparison of structural images. 108
6.23 Comparison of reflectivity images. 109

Chapter 2

Modeling in polar coordinates using one-way wave equations

In this chapter I show how to calculate approximate Green's functions using one-way wave equations in polar coordinates. I use one-way extrapolators to downward or outward continue an initial condition until a solution is obtained in the whole region of interest. The solutions obtained using one-way equations are approximations to the the full Green's functions. However, they contain the information that is usually of greatest interest, the amplitude and phase of the primary arrivals.

2.0.5 Two-way wave equations

The full Green's function is the response to an impulse at the source location. Any modeling program that can represent a impulsive source can be used to calculate the Green's function. The most commonly used algorithms for modeling the full wave-equation in a general medium are finite difference or pseudo-spectral methods. They provide high accuracy and can cope with arbitrary velocity variation, as long as it is on a scale larger than the cell size of the computational grid (Kelly and Marfurt, 1990).

The full Green's function models all events, multiples as well as primaries. This is very valuable if an accurate subsurface model is available but can be a problem if only an approximate model is available. Multiply-scattered events are very sensitive to the positions of discontinuities in the velocity model (Baysal et al., 1984). When a very accurate velocity model is used, a Green's function that is a solution of the full wave-equation is

appropriate. If an accurate velocity model is not available it may be better to ignore or remove the multiply-scattered events. In a situation where the full Green's function is required it will usually be more practical to use a recursive wavefield propagation method that gives the same results but does not explicitly form the Green's function (Whitmore, 1983; Baysal et al., 1985).

2.0.6 One-way wave equations

Most imaging algorithms for surface data assume that the majority of the observed energy is due to single scattering. There are two possible justifications for this. The first is that reflectivities in the the earth are often very small, so that doubly reflected amplitudes are negligible. The second justification is, that since we usually do not have an accurate velocity model we should remove the the multiples by a pre-processing step. The resulting data are then appropriate input for a single-scattering imaging process.

Whenever we use a single-scattering algorithm it is reasonable to use one-way approximation to the full wave equation. These approximations ignore back-scattering in the wavefield. One-way wave equations can be solved in the time-domain but it is often computationally convenient to solve them in the frequency domain. The cost of solving a one-way approximation to the wave equation is much less than solving the full two-way equation.

In this chapter I compare calculation of Green's functions in the usual rectangular coordinate frame and in a polar coordinate frame. Polar coordinates have been successfully used in finite-difference travel time estimation (van Trier and Symes, 1991), but they have not been widely used in calculating full wavefields for oil and gas exploration. They have the advantage of providing a coordinate frame that matches the constant velocity wavefronts. Other non-rectangular coordinate frames have been used in wavefield extrapolation and migration; Li (1986) proposed a linear transformation of the rectangular coordinate frame. Fornberg (1988) uses a conformal mapping to a coordinate frame that is a good match to the velocity model boundaries rather than the wavefield.

In variable-velocity models the wavefronts do not conform exactly to the polar grid but for the most part wave propagation is at low angles to the coordinate frame. This permits the use of low angle paraxial approximations to the one-way wave equation. Paraxial approximations in a polar coordinate frame give an inexpensive method of calculating the Green's functions that can provide the accuracy necessary for imaging high reflector dips.

2.1 Rectangular coordinates

In a 2-D rectangular coordinate frame the constant-density, acoustic, wave equation in the time domain is given by

$$\frac{\partial^2 P}{\partial z^2} + \frac{\partial^2 P}{\partial x^2} = \frac{1}{v^2}\frac{\partial^2 P}{\partial t^2}.$$

When this equation is Fourier transformed over time and x we obtain

$$\frac{\partial^2 P}{\partial z^2} - k_x^2 P = -\frac{\omega^2}{v^2} P$$

or,

$$\frac{\partial^2 P}{\partial z^2} = \left[k_x^2 - \frac{\omega^2}{v^2}\right] P.$$

If we assume a solution of the form

$$P(z) = P(z_0) e^{ik_z(z-z_0)},$$

we find

$$k_z = \pm\sqrt{\frac{\omega^2}{v^2} - k_x^2}\ . \tag{2.1}$$

By choosing the positive square root for positive frequencies we transform the two-way wave equation into a one-way equation. The one-way equation is the equation for waves that propagate downwards as time increases. Given a solution at one depth level $P(z)$ we can extrapolate it to a new depth level using a pure phase shift $P(z+\Delta z) \approx P(z)e^{ik_z \Delta z}$.

Using this method we can propagate an initial condition specified at $z = 0$ to any depth by applying suitable phase shifts at each depth level. This method was originally described by Gazdag (1978). The major limitation of this method is that the velocity field is taken to be constant over the interval z to $z + \delta z$. This will be untrue in the presence of lateral variation of velocity, or strong vertical gradients.

2.1.1 Initial conditions in rectangular coordinates

For surface seismic experiments we require Green's functions that are the response to an impulse at a single point on the surface. However the phase shift algorithm in rectangular coordinates requires initial conditions at all locations on the surface, $z = 0$. Since horizontal waves, reflected waves, and overturned waves can all contribute to the surface wavefield it appears that the full solution must already be known in order to supply these

initial data. To avoid this problem I exclude dips that are close to the horizontal. Only events traveling at less than some angle to the vertical, say 80 degrees, are propagated. The initial condition is then just an impulse at the source location that is dip-filtered to the appropriate dip range. While this dip-limited impulse does not reproduce the Green's function correctly at high dips, it should be adequate for the dip ranges typical in most seismic data.

Figure 2.1 shows the amplitude and phase plots for a mono-frequency Green's function calculated for a constant-velocity medium. The amplitude should be radially symmetric but it diminishes near the surface because of the dip-limitation of the initial condition. Figure 2.2 shows one time slice through the full Green's function in the (x, z, t) domain. This was calculated by inverse Fourier transforming a complete set of mono-frequency Green's functions. The dip-limitation in the initial conditions is clearly visible as an amplitude decay of the wavefront at steeper angles.

Because the simple one-way phase shift method only propagates energy downwards, it cannot correctly model overturned waves. Claerbout (1985) explained how to overcome this problem by saving the upgoing energy at each depth step, and then in a later upwards extrapolation pass the upgoing energy is propagated to the surface. This method of modeling overturned waves requires more computation than a simple downward extrapolation. This cost would appear to be double but in most cases it is much less as only a small range of wavenumbers needs to used in the upwards extrapolation (Hale et al., 1992).

2.2 Polar coordinates

The problems associated with extrapolating overturned waves and specifying initial conditions can be bypassed by calculating the Green's functions in polar coordinates. Van Trier and Symes (1991) use polar coordinates for similar reasons in their finite-difference solution to the eikonal equation.

I will follow exactly the same steps in deriving the algorithm in polar coordinates as I did in rectangular coordinates. In a 2-D polar coordinate frame, the wave equation is,

$$\frac{\partial^2 P}{\partial r^2} + \frac{1}{r}\frac{\partial P}{\partial r} + \frac{1}{r^2}\frac{\partial^2 P}{\partial \theta^2} = \frac{1}{v^2}\frac{\partial^2 P}{\partial t^2}$$

When this equation is Fourier transformed over t and θ we obtain,

$$\frac{\partial^2 P}{\partial r^2} + \frac{1}{r}\frac{\partial P}{\partial r} - \frac{1}{r^2}k_\theta^2 P = -\frac{\omega^2}{v^2}P$$

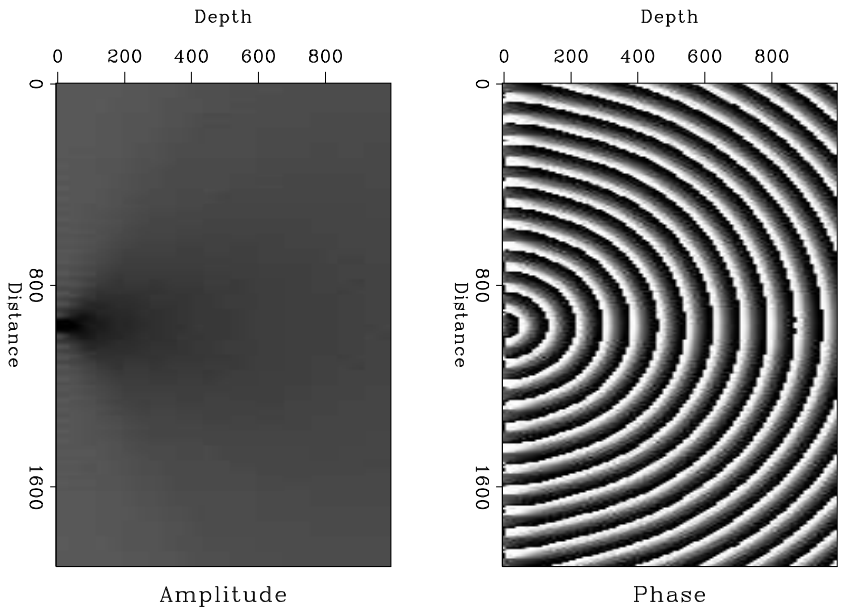

FIG. 2.1. Amplitude (left) and phase (right) for a mono-frequency Green's function calculated in rectangular coordinates. This is a constant-velocity medium with a dip-filtered impulse as the initial condition. Polgreens-rect-one [CR]

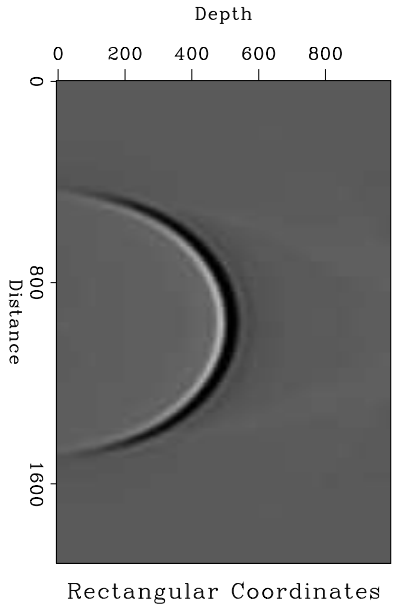

FIG. 2.2. A time slice through the (x, z, t) Green's function calculated by inverse transforming a complete range of mono-frequency Green's functions calculated in rectangular coordinates. Polgreens-rect-all [CR]

If we assume a solution of the form,

$$P(r) = P(r_0)e^{ik_r(r-r_0)}, \tag{2.2}$$

we find,

$$k_r = \frac{i}{2r} \pm \sqrt{\frac{\omega^2}{v^2} - \frac{k_\theta^2}{r^2} - \frac{1}{4r^2}}$$

Thus given a wavefield at some radius r we can propagate it to a new radius using,

$$P(r+\Delta r) = P(r)\exp\left(-\frac{\Delta r}{2r}\right)\exp\left(i\sqrt{\frac{\omega^2}{v^2} - \frac{k_\theta^2}{r^2} - \frac{1}{4r^2}}\Delta r\right)$$

The real part of this expression controls the amplitude decay due to increasing wavefront radius and the imaginary part gives the phase shift. In a constant-velocity medium the amplitude term can be integrated to give the familiar $1/\sqrt{r}$ amplitude decay:

$$P(r) = P(r_0)\prod_{r_0}^{r}\exp\left(-\frac{\Delta r}{2r}\right) exp\left(i\sqrt{\frac{\omega^2}{v^2} - \frac{k_\theta^2}{r^2} - \frac{1}{4r^2}}\Delta r\right)$$

$$\begin{aligned} |P(r)| &= P(r_0)\exp\left(-\int_{r_0}^{r}\frac{1}{2r'}\,dr'\right) \\ &= P(r_0)\exp\left(-[1/2\,\log(r')]_{r_0}^{r}\right) \\ &= P(r_0)[r/r_0]^{-1/2} \end{aligned}$$

2.2.1 Initial conditions in polar coordinates

The initial conditions are not supplied at the point $r = 0$, but rather at some finite initial radius r_0. The region between the origin and r_0 is assumed to be homogeneous. A simple approximate initial condition is,

$$P(r_0, \theta, \omega) = \frac{1}{\sqrt{r_0}}\, exp\left(i\omega\frac{r_0}{v}\right).$$

Figure 2.3 shows amplitude and phase plots for a mono-frequency Green's function calculated using equation (2.2) for a constant-velocity medium. The polar coordinate data has been re-interpolated onto the same rectangular grid as the rectangular coordinate data. The amplitude is now more uniform for all dips. Figure 2.4 shows one time slice through the full Green's function in the (x, z, t) domain. The result is a much more accurate representation of the wavefront. There is no dip dependent amplitude variation along the wavefront and the dips go all the way to 90° because dip-filtering of the initial impulse was not required.

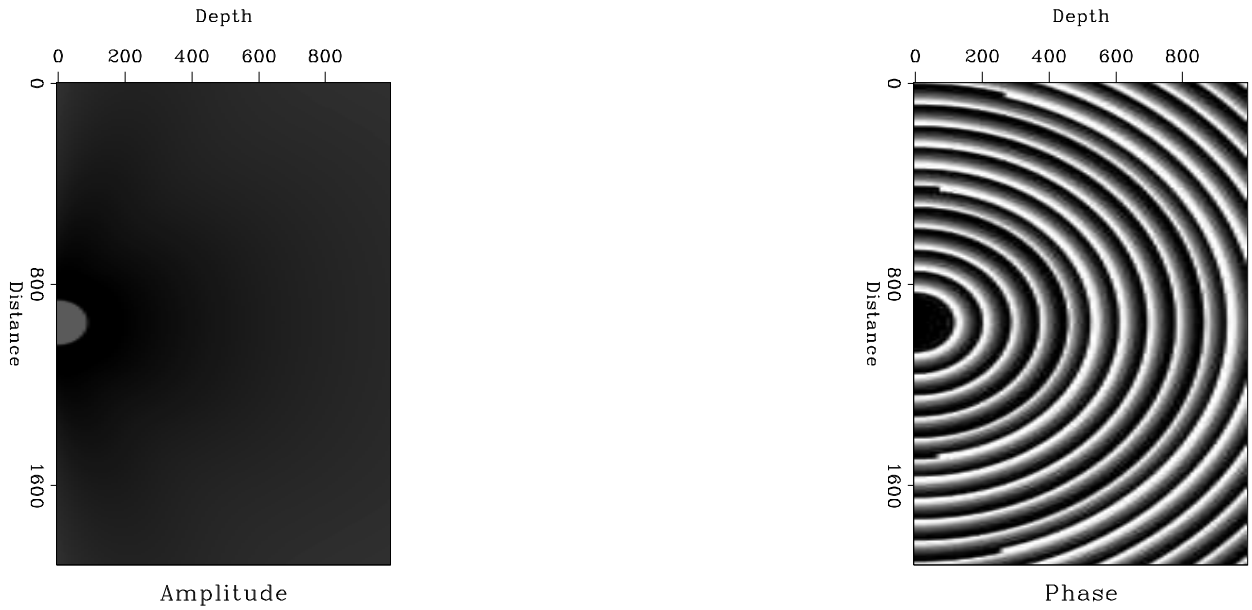

FIG. 2.3. Amplitude (left) and phase (right) for a mono-frequency Green's function calculated in polar coordinates. The initial condition is a constant value on a semi-circle of radius 80m. Polgreens-pol-one [CR]

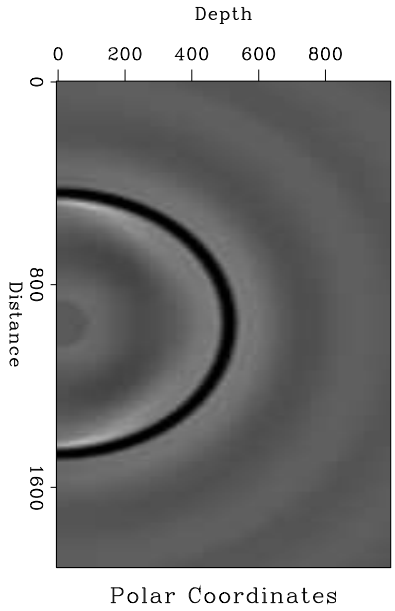

FIG. 2.4. A time slice through the (x, z, t) Green's function calculated by inverse transforming a complete range of mono-frequency Green's functions calculated in polar coordinates. Polgreens-pol-all [CR]

2.3 Handling velocity variation

The two phase-shift schemes are eminently suited for use with a constant velocity model or a model which varies only in the direction in which the data is extrapolated. For rectangular coordinates this is a $v(z)$ model; for polar coordinates a $v(r)$ model is implied. When the velocity model is not of a suitable form, a more complicated algorithm must be used.

In many cases a $v(z)$ model is geologically reasonable, but this is rarely true of a $v(r)$ model (except in the special case of a source at the center of the earth). Thus, one disadvantage of working in polar coordinates is that the simple phase-shift algorithm cannot be used for a $v(z)$ model.

2.3.1 Phase-shift plus interpolation

The simplest extension to the phase shift algorithm is "phase-shift plus interpolation" (PSPI) (Gazdag and Sguazzero, 1984). This algorithm approximates the extrapolation of the wavefield in a spatially varying velocity field by interpolating between the results of a set of constant-velocity extrapolations. The interpolation is performed locally in space. This method therefore requires an inverse Fourier transform of each constant-velocity panel back to the space domain (x or θ), and a forward transform of the interpolated result to return to the wavenumber domain, for each extrapolation step in z or r.

I use the simplest form of the PSPI algorithm which uses only two constant-velocity extrapolations. The two velocities are the minimum and maximum velocity at the current depth or radius.

In rectangular coordinates,

$$
\begin{aligned}
P_1(z+\Delta z, k_x) &= P(z,k_x) e^{ik_z(v_{min},k_x)\Delta z} \\
P_2(z+\Delta z, k_x) &= P(z,k_x) e^{ik_z(v_{max},k_x)\Delta z} \\
P_1(z+\Delta z, x) &= \mathcal{FT}_x^{-1}\left\{P_1(z+\Delta z, k_x)\right\} \\
P_2(z+\Delta z, x) &= \mathcal{FT}_x^{-1}\left\{P_1(z+\Delta z, k_x)\right\} \\
P(z+\Delta z, x) &= P_1(z+\Delta z, x)\frac{v_{max}-v(x)}{v_{max}-v_{min}} + P_2(z+\Delta z, x)\frac{v(x)-v_{min}}{v_{max}-v_{min}} \\
P(z+\Delta z, k_x) &= \mathcal{FT}_x\left\{P(z+\Delta z, x)\right\}
\end{aligned}
$$

In polar coordinates the algorithm has the same form with r replacing z.

Figure 2.5 shows the results of modeling in a medium which has a linear gradient in x and z. The velocity field in this model is $v(x,z) = v_0 + \alpha(x - x_0) + \beta(z - z_0)$. The plot on the left is computed in rectangular coordinates and the one on the right in polar coordinates. They both show an asymmetric wavefront produced by the velocity gradient. The polar coordinate result contains energy at higher dips than the rectangular coordinate result because it does not start with a dip-filtered impulse.

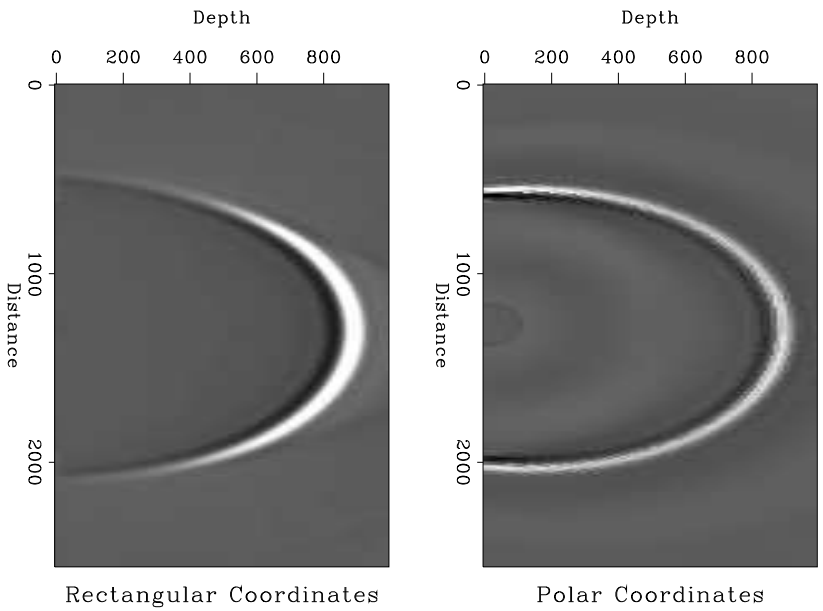

FIG. 2.5. A time slice from modeling in a linear gradient medium. The velocity field has a gradient of 5 $(ms^{-1})/m$ in depth and 5 $(ms^{-1})/m$ in x. The result on the left is computed in rectangular coordinates, the one on the right is computed in polar coordinates. Polgreens-grad-both [CR]

2.3.2 Paraxial approximations

A common way of extrapolating the wavefield in a variable velocity medium is to use a paraxial approximation to the wave equation, (Claerbout and Doherty, 1972). The well-known 45° paraxial approximation to equation (2.1) in the space domain is

$$\frac{\partial P}{\partial z} = i\frac{\omega}{v}P - \frac{\frac{iv}{2\omega}\frac{\partial^2}{\partial x^2}}{1 + \frac{v^2}{4\omega^2}\frac{\partial^2}{\partial x^2}}P$$

Following the usual splitting procedure this becomes,

$$\left(1 - \frac{v^2}{4\omega^2}\frac{\partial^2}{\partial x^2}\right)\frac{\partial Q}{\partial z} = \frac{iv}{2\omega}\frac{\partial^2 Q}{\partial x^2} \tag{2.3}$$

where $Q(x,z)$ is the wavefield in a time-retarded coordinate frame, followed by conversion back to the regular time coordinate frame.

$$P(z+\Delta z) = Q(z+\Delta z)\exp(i\int \frac{\omega}{v}\Delta z).$$

Discretization in space of equation (2.3) using the Crank-Nicholson scheme results in a tridiagonal set of equations to be solved in order to propagate the wavefield from a level z to $z+\Delta z$.

The equations in polar coordinates can be similarly transformed; the paraxial approximation is,

$$\frac{\partial P}{\partial r} = \left(\frac{-1}{r^2} + i\sqrt{\alpha}\right) P - \frac{\frac{i\sqrt{\alpha}}{2r^2}\frac{\partial^2}{\partial\theta^2}}{1-\frac{\alpha}{4r^2}\frac{\partial^2}{\partial\theta^2}} P$$

where,

$$\alpha = \sqrt{\frac{\omega^2}{v^2} - \frac{1}{4r^2}}$$

After splitting this becomes,

$$\left(1 - \frac{\alpha}{4r^2}\frac{\partial^2}{\partial\theta^2}\right)\frac{\partial Q}{\partial r} = \frac{i\sqrt{\alpha}}{2r^2}\frac{\partial^2 Q}{\partial\theta^2}$$

followed by,

$$P(r+\Delta r) = Q(r+\Delta r)\exp\left(\frac{-1}{r^2} + i\sqrt{\alpha}\Delta r\right)$$

Again discretization of the first equation yields a tridiagonal set of equations to be solved for each depth step.

The results of using these two schemes in a constant-velocity model are shown in figure 2.6. The 45° approximation is clearly visible in the rectangular coordinate data. Since the wavefront propagates at zero degrees to the polar coordinate frame, the polar data does not show any artifacts due to the 45° approximation.

Low order paraxial approximations will not accurately model events that propagate at high angles to the coordinate frame of the finite-difference mesh. In rectangular coordinates this means that near-vertical waves should be propagated using depth extrapolation, and near-horizontal waves would be best modeled using lateral-extrapolation. If the problem to be solved is one of downward continuing surface data that contains events that are mostly near vertical (e.g. zero offset migration for moderate reflector dips), a rectangular coordinate frame and depth extrapolation are appropriate. On the other hand if the problem is one of modeling a near-circular outgoing wavefront from a point source, then polar coordinates and outward radial extrapolation are superior.

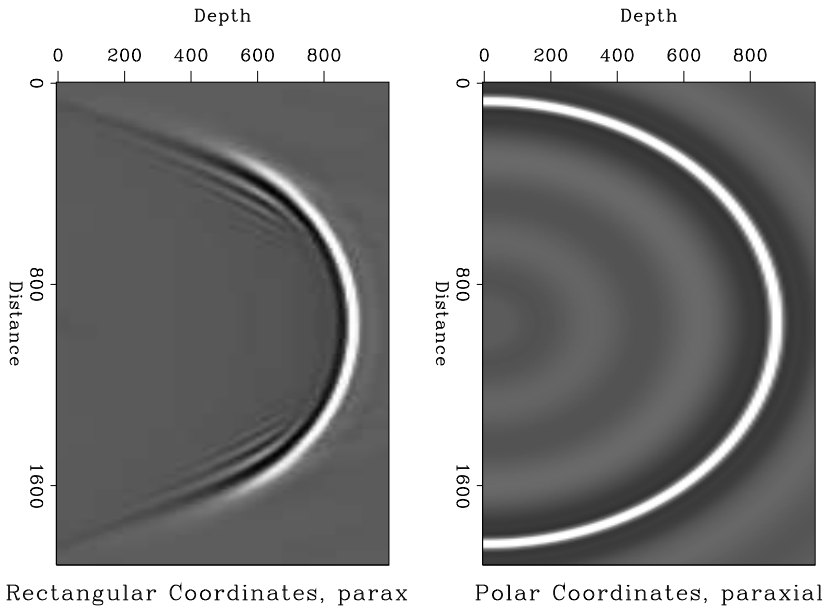

FIG. 2.6. Modeling in a constant-velocity medium using the 45° paraxial approximation. The plot on the left was computed in rectangular coordinates the plot on the right was computed in a polar coordinate frame. Polgreens-parax-both [CR]

2.4 Problems with polar coordinates

The major disadvantage of using a polar coordinate frame is that it is only suitable for calculating the Green's function for a single point. When Green's functions are to be combined, they must be interpolated to a common coordinate frame. In contrast, data from rectangular coordinate frames centered at different points can be combined by a simple shift along the coordinate axes.

All of the polar coordinate figures in this paper have been interpolated onto the same mesh as the rectangular coordinate frame data using a bilinear interpolator. In some figures, the interpolation step has produced clearly visible artifacts. The polar data has a "rough" quality that the rectangular coordinate data does not. The problem is most severe when the radius is large. In these cases the spacing between the different radii is much larger than the largest spacing on the rectangular grid. In these regions aliasing may become a problem if the waves propagate at an high angle to the polar grid.

Another problem is that the trial solution used in equation (2.2) is an approximate solution. It is only valid in the far field and breaks down at low frequency and small

radius. This can be seen by examining the formula for the radial wavenumber,

$$k_r = \frac{i}{2r} \pm \sqrt{\frac{\omega^2}{v^2} - \frac{k_\theta^2}{r^2} - \frac{1}{4r^2}}\,.$$

The expression inside the square-root becomes negative for all values of k_θ when $r < 2\omega/v$. This provides a lower limit to the radius at which to specify the initial condition ($r > \lambda/2$). In practice it is advisable to make the initial radius a least two wavelengths of the lowest frequency.

2.4.1 More complicated coordinate frames

The principal advantage of polar coordinates is that the computational grid is a better match to the wavefront than a rectangular grid. Because of this we are able to accurately extrapolate high dips with a 45° extrapolator. This principle could be carried further.

In a $v(z)$ medium we could use one coordinate that followed $v(z)$ raypaths, instead of straight radial lines, and a second coordinate that was along contours of equal traveltime. In this medium, if we had chosen the correct velocity model, the wavefront would always conform to surfaces with a constant first coordinate, and a very low angle extrapolator could be used. There are disadvantages to this coordinate system too: the wave equation becomes even more complicated, and the derivatives in "r" and "θ" are not decoupled as they are in the polar system. The tradeoff to be made is between having a more complicated wave equation and being able to use a lower accuracy paraxial approximation.

In a general velocity medium we could use a local coordinate system that followed all the rays and then use a zero degree extrapolator to propagate the energy. This would be something very close to the methods of paraxial rays (e.g. Beydoun and Keho (1987), Červený et al.(1984)) or Gaussian beams (e.g. Červený (1986), Červený et al. (1982)). One disadvantage of these methods is that the energy always propagates along the asymptotic ray. In contrast when using a paraxial wave equation, whatever coordinate system you choose, energy may propagate at a moderate angle to the coordinate system. In a geometrically dispersive medium the asymptotic ray may not be the true "ray" at low frequencies (Biondi, 1992). Use of a paraxial wave equation allows the modeled energy to take different paths at different frequencies.

Another feature of ray-based schemes is that you must trace the rays for all the arrivals that you wish to contribute to your output. If you wish the output to contain reflection or diffraction energy you must trace rays corresponding to those wavefronts. This might

be regarded as an advantage if you are only interested in specific events. However, the polar coordinate system requires no ray tracing at all and, for many velocity models, a 45° wave equation on the polar grid will propagate all events of interest accurately.

I hypothesize that the greatest jump in quality comes from the change from rectangular coordinates to polar coordinates. Further refinements may be more effort than they are worth. However, this is obviously a subject worthy of further investigation.

2.5 Some examples

Figure 2.7 shows the modeling results for a $v(z)$ medium with a strong velocity gradient ($10ms^{-1}/m$). In this medium the wavefronts eventually overturn. My rectangular-coordinate modeling code does not produce the overturned waves because the wavefield is always extrapolated downwards and any energy in the evanescent zone (with a dip greater than 90°) is removed at each downwards extrapolation step. However it is surprising to see energy in the rectangular coordinate frame that is apparently upgoing. This may be a byproduct of the high velocity gradient. The energy has a phase slowness that points horizontally but a group slowness that points upwards. There is less energy in the "overturned" region than there should be, because the true overturned energy has not been modeled. The two polar coordinate frames show the correct amount of overturned energy. In this particular example the 45° result may be better than the PSPI result in polar coordinates. This is because the very strong gradient is not well handled by the PSPI algorithm. The gradient affects the polar coordinate PSPI code because there is a strong gradient in θ, even though there in no gradient in x.

Figure 2.8 shows another result with upgoing energy. In this case the energy may not be desirable. The model is a two layer medium with a step function in velocity at 300m. The rectangular coordinate frame phase shift result shows only downgoing waves. In contrast the two polar coordinate results display a small piece of reflected energy. This is energy that is upgoing, but still outgoing! Once the angle of incidence exceeds 45° to the vertical the reflected energy is propagated outwards in the polar coordinate frame. There is also some dispersed energy in the 45° result. This is probably due to reflected energy that travels at more than 45° to the polar grid and is thus poorly modeled.

Figure 2.9 shows the result of modeling in a medium with a small low velocity anomaly. The anomaly is a Gaussian blob with a half width of 100m. Apart from the loss of high

dips in the rectangular coordinate frame, all three methods produce fairly similar results. The polar coordinate, 45° wave equation, result is the best of these because it can handle both, steep dips, and velocity variation. It was also the cheapest to produce.

2.6 Summary

Mono-frequency Green's functions can be computed using phase shift or finite-difference schemes in either rectangular or polar coordinates. In polar coordinates the 45° $\omega - \theta$ approximation will give accurate high dip results at low dip cost. The $\omega - \theta$ domain method also handles laterally variable velocity more robustly than the PSPI method, which is required for high dip accuracy in rectangular coordinates.

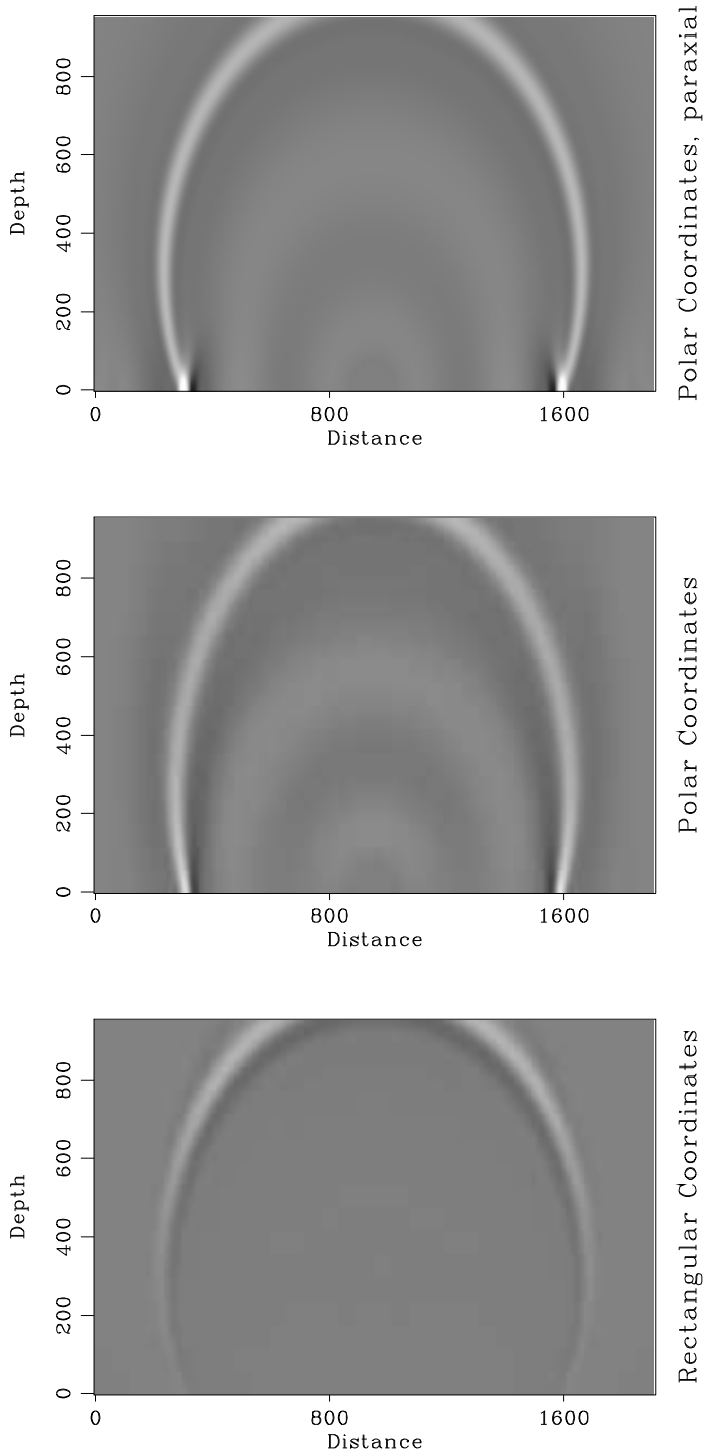

FIG. 2.7. Modeling in a linear velocity gradient in depth. A snapshot of the Green's function, depth is plotted upwards. The plot on the bottom was computed by PSPI in rectangular coordinates. The plot in the middle was computed by PSPI in a polar coordinate frame. The plot on the top was computed using the 45° wave equation in polar coordinates. Polgreens-over-three [CR]

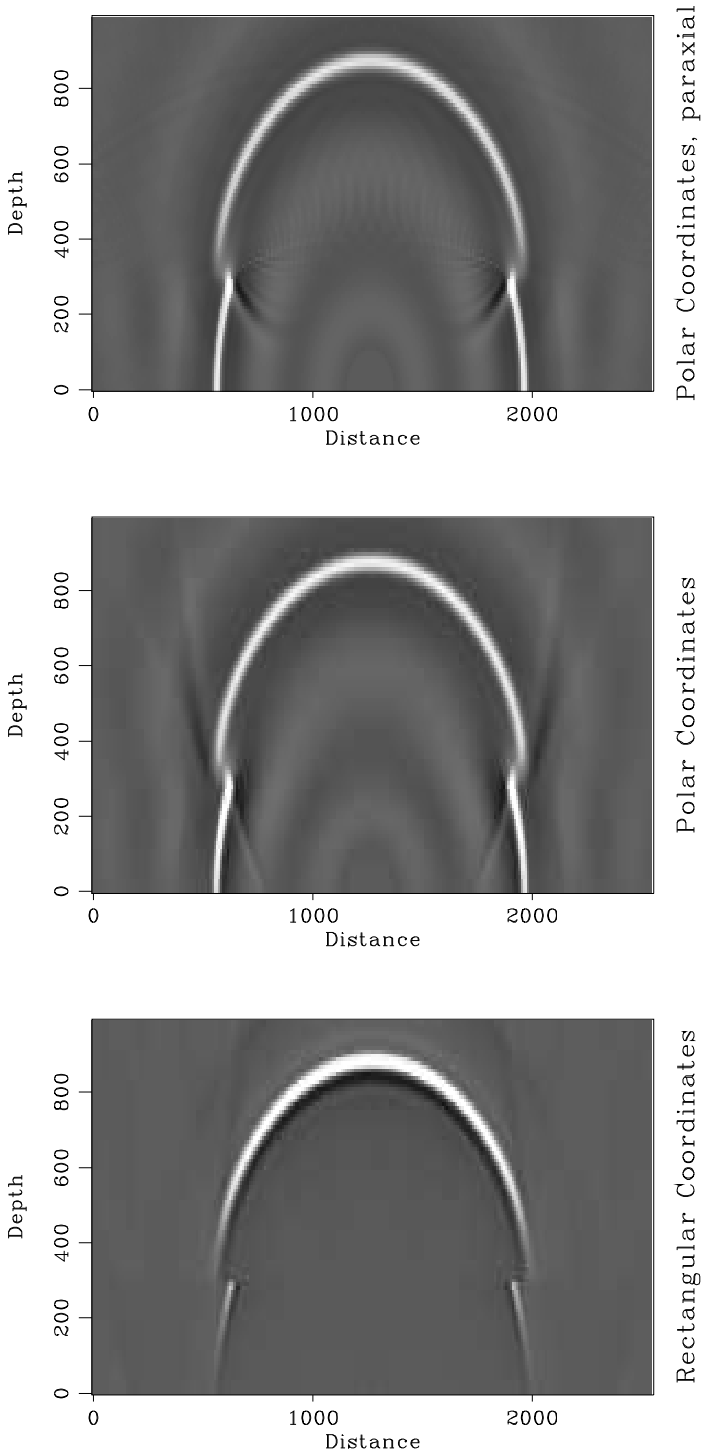

FIG. 2.8. Modeling in a two layer model. A snapshot of the Green's function, depth is plotted upwards. The plot on the bottom was computed by PSPI in rectangular coordinates. The plot in the middle was computed by PSPI in a polar coordinate frame. The plot on the top was computed using the 45° wave equation in polar coordinates. Polgreens-refl-three [CR]

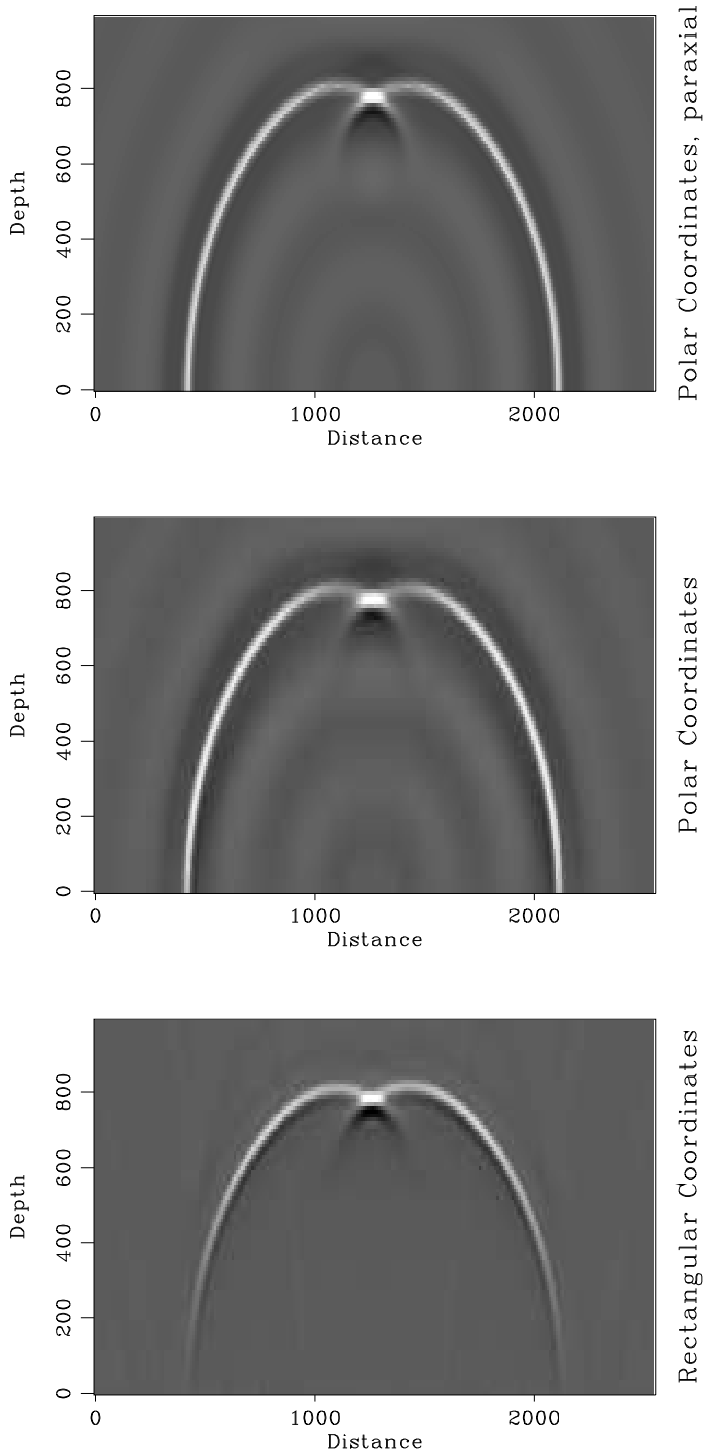

FIG. 2.9. Modeling in medium with a Gaussian anomaly. A snapshot of the Green's function, depth is plotted upwards. The plot on the bottom was computed by PSPI in rectangular coordinates. The plot in the middle was computed by PSPI in a polar coordinate frame. The plot on the top was computed using the 45° wave equation in polar coordinates. Polgreens-blob-three [CR]